Cell Reports

Optogenetic silencing of medial septal GABAergic neurons disrupts grid cell spatial and temporal coding in the medial entorhinal cortex

Graphical abstract

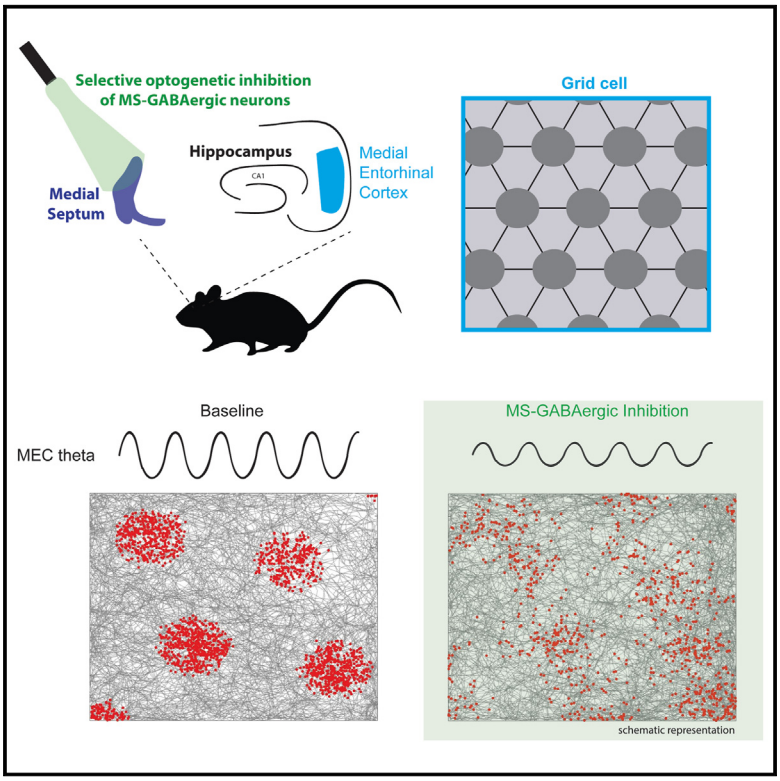

Authors

Jennifer C. Robinson, Johnson Ying, Michael E. Hasselmo, Mark P. Brandon

Correspondence

jenniferclaire.robinson@gmail.com (J.C.R.), mark.brandon@mcgill.ca (M.P.B.)

In brief

Robinson et al. demonstrate that optogenetic inhibition of MS-GABAergic neurons disrupts the spatial and temporal coding of grid cells. Grid cell spatial periodicity is perturbed not only during optogenetic inhibition but also during short recovery periods. Longer recovery periods following optogenetic inhibition facilitate the recovery of grid cell periodicity.

Highlights

- Medial septum (MS)-GABAergic inhibition reduces theta rhythms
- MS-GABAergic inhibition disrupts grid cell spatial periodicity and theta phase precession
- Theta rhythm is restored immediately after MS-GABAergic inhibition
- Grid cell spatial coding takes longer (60 s) to recover from MS-GABAergic inhibition

Robinson et al., 2024, Cell Reports *43*, 114590
August 27, 2024
https://doi.org/10.1016/j.celrep.2024.114590

CellPress

Cell Reports

CellPress
OPEN ACCESS

Report

Optogenetic silencing of medial septal GABAergic neurons disrupts grid cell spatial and temporal coding in the medial entorhinal cortex

Jennifer C. Robinson,[1,5,*] Johnson Ying,[2,3] Michael E. Hasselmo,[1,4] and Mark P. Brandon[2,3,4,*]
[1]Center for Systems Neuroscience, Department of Psychological and Brain Sciences, Boston University, Boston, MA, USA
[2]Department of Psychiatry, Douglas Hospital Research Centre, McGill University, Montreal QC, Canada
[3]Integrated Program in Neuroscience, McGill University, Montreal, QC, Canada
[4]These authors contributed equally
[5]Lead contact
*Correspondence: jenniferclaire.robinson@gmail.com (J.C.R.), mark.brandon@mcgill.ca (M.P.B.)
https://doi.org/10.1016/j.celrep.2024.114590

SUMMARY

The hippocampus and medial entorhinal cortex (MEC) form a cognitive map that facilitates spatial navigation. As part of this map, MEC grid cells fire in a repeating hexagonal pattern across an environment. This grid pattern relies on inputs from the medial septum (MS). The MS, and specifically GABAergic neurons, are essential for theta rhythm oscillations in the entorhinal-hippocampal network; however, the role of this population in grid cell function is unclear. To investigate this, we use optogenetics to inhibit MS-GABAergic neurons and observe that MS-GABAergic inhibition disrupts grid cell spatial periodicity. Grid cell spatial periodicity is disrupted during both optogenetic inhibition periods and short inter-stimulus intervals. In contrast, longer inter-stimulus intervals allow for the recovery of grid cell spatial firing. In addition, grid cell phase precession is also disrupted. These findings highlight the critical role of MS-GABAergic neurons in maintaining grid cell spatial and temporal coding in the MEC.

INTRODUCTION

The medial entorhinal cortex (MEC) contains a diversity of spatially modulated neurons that include grid cells that fire at regular spatial intervals to form a hexagonal pattern of spatial fields across an environment.[1–3] Current theories predict that these repetitive patterns support navigation and memory encoding by providing self-motion-based information represented in a metric of space.[1,4–6] The networks that support grid cell spatial periodicity include the anterior thalamic nuclei,[7] the hippocampus,[8] and the medial septum (MS).[9,10] The MS is critical for theta rhythm generation in the hippocampus and the MEC. Lesions or inactivation of the MS disrupt theta oscillations in the hippocampal and entorhinal networks[11–13] and cause significant spatial memory deficits.[14,15] Importantly, the MS consists of three distinct cell types: GABAergic, glutamatergic, and cholinergic neurons.[16] It remains unclear which cell type supports grid cell spatial firing. Previous data suggest that MS-GABAergic neurons are the central pacemakers of theta rhythm activity (6–12 Hz) in the MEC and hippocampus, as demonstrated by their burst firing pattern at theta frequencies *in vivo*,[17] their temporal lead ahead of hippocampal theta activity,[18] and their primary contact with hippocampal and entorhinal interneurons[19,20] that pace theta oscillations.[21] Optogenetic activation of the MS-GABAergic subpopulation of parvalbumin (PV) neurons entrains hippocampal and MEC oscillations[22–24] while silencing septal GABAergic neurons results in a large decrease in the power of endogenous theta oscillations during open field exploration and rapid eye movement sleep.[25,26] It is well established that MEC grid cell periodicity relies on inputs from the MS,[9,10] but recent studies call into question the necessity of theta oscillations for grid cell periodicity.[24,27] Optogenetic activation of GABAergic subpopulation PV neurons in the MS paces ongoing oscillation well above the theta range but does not disrupt the grid cell spatial pattern.[24,27] To more directly test whether MS-GABAergic-driven theta oscillations support grid cell firing, we used optogenetic inhibition to selectively silence MS-GABAergic neurons to reduce endogenous theta oscillations to examine their contribution to both spatial and temporal coding of grid cells in the MEC.

RESULTS

Selective inhibition of MS-GABAergic neurons in the MS decreases the power of theta oscillations and grid cell periodicity

To target MS-GABAergic neurons in the MS, the Archaerhodopsin-3 variant ArchT[28] was selectively expressed in the MS (Figure 1A). Selectivity was driven by a Cre-dependent adeno-associated virus injected into the MS of VGAT^{cre} mice (STAR Methods). An optic fiber was positioned above the MS for light delivery, while both single-unit and local field potential

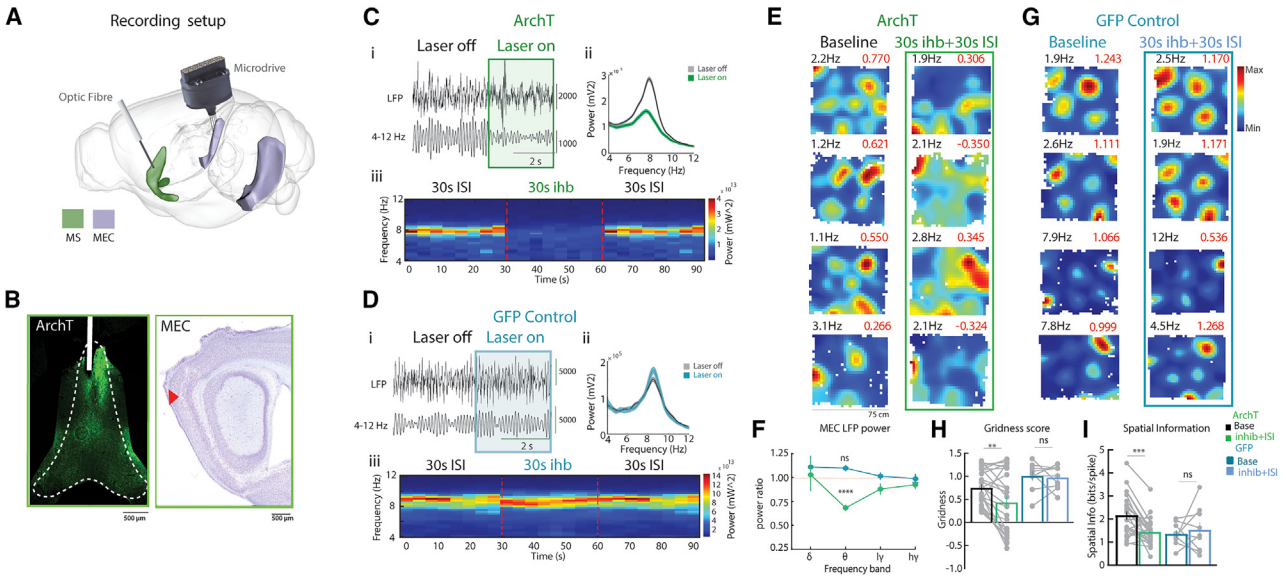

Figure 1. Optogenetic targeting of MS-GABAergic neurons with archaerhodopsin reduces endogenous theta oscillations and disrupts GC spatial firing

(A) Illustration of the stimulation and recording setup with an optic fiber placed above the MS at a 5°–6° angle and a 4-tetrode microdrive placed above the MEC. The illustration was modified from https://scalablebrainatlas.incf.org/.

(B) Left: example image of virus expression of adeno-associated virus-ArchT-GFP, shown in green, in a coronal section of the MS. Right: example electrode track in the sagittal section of the MEC (scale bars, 500 μm).

(C) ArchT example of (i) raw (top) and filtered LFP (bottom) during laser-off and laser-on periods, (ii) example power spectrum for a full recording session with repeated 30-s ihb (green) and 30-s ISI periods (gray), and (iii) average spectrogram corresponding to (ii) within the theta range for 30-s ISI and 30-s laser-on inhibition (ihb) periods.

(D) GFP control example of (i) raw (top) and filtered LFP (bottom) during laser off and laser on; (ii) example power spectrum for a full, ∼40-min recording session with repeated 30-s ihb (blue) and 30-s ISI periods (gray); and (iii) averaged spectrogram corresponding to (ii) within the theta range for 30-s ISI and 30-s laser on ihb periods.

(E) Example rate maps for cells recorded in a 75 × 75 cm square open field environment during baseline (left) and combined 30-s silencing followed by a 30-s inter-stimulus interval (ISI) (right), with peak firing rate shown in black and gridness score in red above each rate map for ArchT group.

(F) Proportion of 30-s ihb of delta, theta, and low- and high-gamma power compared to 30-s ISI periods for ArchT (green) and GFP (blue) (ArchT, $n = 15$; GFP, $n = 9$ recording sessions; one-sample Wilcoxon test, $p < 0.0001$).

(G) Example rate maps for cells recording across baseline (left) and combined 30-s silencing followed by 30-s ISI (right) for GFP controls, with peak firing rate shown in black and gridness score in red above each rate map.

(H) Gridness score for baseline and stimulation conditions for both the ArchT and GFP groups (ArchT, $n = 25$ cells; GFP, $n = 9$ cells; Wilcoxon matched-pairs signed-rank test, $p < 0.01$).

(I) Spatial information score for baseline and stimulation conditions for both the ArchT and GFP groups (ArchT, $n = 25$ cells; GFP, $n = 9$ cells; Wilcoxon matched-pairs signed-rank test; $p < 0.001$).

ns, non-significant; *$p < 0.05$, **$p < 0.01$, ***$p < 0.001$, ****$p < 0.0001$. Unless indicated otherwise, all results are presented as mean ± SEM.

(LFP) recordings were recorded in the MEC (Figure 1B). Consistent with prior work,[25,26] MS-GABAergic neuron inhibition resulted in a clear decrease in the power of endogenous MEC theta oscillations (Figure 1C; $n = 8$ experimental animals). In contrast, green fluorescent protein (GFP) control animals show a slight but non-significant increase in theta power during laser-on periods (Figure 1D; $n = 3$ GFP control animals). Only theta power was found to be significantly affected by MS-GABAergic inhibition (theta mean, 0.6915 ± 0.0287, one-sample Wilcoxon test, $p < 0.0001$) (Figure 1F). The optogenetic inhibition protocol consisted of 30-s laser-on inhibition periods (labeled inhibition [ihb] in the figures) alternating with 30-s inter-stimulus intervals (ISIs) repeated throughout the full recording session (STAR Methods).

To quantify the extent to which grid cells were affected by MS-GABAergic ihb, the gridness score (a measure of hexagonal spatial periodicity in the rate map; STAR Methods) was assessed during the baseline recording session, ihb periods, and ISI periods. The gridness score was decreased significantly during the stimulation recordings compared to baseline (mean ± SEM, Wilcoxon matched-pairs signed-rank test; baseline mean 0.74 ± 0.077, stimulation (stim) mean 0.43 ± 0.14, $p < 0.01$, $n =$ 25 grid cells [GCs] recorded across 8 animals) (Figures 1E, 1H, and S1), while no significant difference was found in GFP controls (mean ± SEM, Wilcoxon matched-pairs signed rank-test; baseline mean 1.01 ± 0.10, stim mean 0.97 ± 0.083, $p = 0.94$, $n = 9$ GCs) (Figures 1G and S2). Although the mean gridness score was significantly decreased, GCs expressed a heterogeneity in their response; some cells maintained their periodic firing, while others were disrupted (see point distribution in Figure 1H). It is possible that cells that maintain their spatial firing would require extended periods of MS-GABAergic ihb to elicit a disruption in spatial periodicity. Alternatively, this subset of

GCs may be less reliant on theta oscillations, consistent with reports where GCs maintained their periodicity firing without endogenous theta.[24,29] Considering that muscimol-mediated septal inactivation results in both the loss of theta oscillations and periodic firing in all GCs,[9,10] we predict that certain GCs may require a more prolonged disruption of theta ihb than performed in this study. In addition, we observed similar results but with less variability when measuring spatial information content (means ± SEM, Wilcoxon matched-pairs signed-rank test; ArchT baseline mean 2.151 ± 0.1773, stim mean 1.433 ± 0.1162, $p < 0.001$, $n = 25$ GCs; GFP baseline mean 1.349 ± 0.1598, stim mean 1.527 ± 0.3261, $p = 0.9102$, $n = 9$ GCs) (Figure 1I). Consistent with previous findings,[9] head direction and other non-grid spatially modulated neurons were unaffected by the stimulations (Figures S3 and S4); however, we did observe a multifield non-GC where the spatial field was disrupted due to MS-GABAergic ihb (Figure S3, example 1). These results demonstrate that MS-GABAergic neurons facilitate GC spatial periodicity and provide supporting evidence for the essential role of theta oscillations in maintaining the spatial firing pattern of GCs.

GC spatial firing does not recover immediately with the return of theta oscillations

To further examine the relationship between GC periodicity and theta oscillations, we split and concatenated recording sessions separately into ihb and ISI periods (Figure 2A). Compared to the baseline recording, GC periodicity was significantly disrupted during both the ihb and ISI periods (mean ± SEM, baseline mean 0.74 ± 0.076, 30-s ihb mean 0.30 ± 0.10, 30-s ISI mean 0.31 ± 0.12, Friedman test, $p < 0.0001$ with Dunn's multiple-comparisons test, baseline vs. 30-s ihb $p < 0.001$, baseline vs. 30-s ISI $p < 0.001$, 30-s ihb vs. 30-s ISI $p > 0.9999$) (Figure 2B). The absence of spatial periodicity in the 30-s ISI period when endogenous theta rhythms returned (as shown in Figure 1Ciii) provides insights into the time that the GC network requires to recover and return to a normal grid-firing pattern following MS-GABAergic ihb. These data demonstrate that short bouts of theta oscillations are not sufficient to support GC spatial firing and that network-wide dynamics may require more time to recover following MS-GABAergic ihb.

We further examined the general firing properties of GCs and found that mean firing was significantly higher during the 30-s ISI period compared to 30-s ihb (mean ± SEM, mean firing [Hz] baseline mean 1.13 ± 0.19, 30-s ihb mean 1.14 ± 0.13, 30-s ISI mean 1.31 ± 0.16, Friedman test $p < 0.05$ with Dunn's multiple-comparisons test, baseline vs. 30-s ihb, $p > 0.999$; baseline vs. 30-s ISI, $p = 0.0589$, 30-s ihb vs. 30-s ISI, $p < 0.05$) (Figure 2C). This could be due to rebound activity following the ihb period. Controls expressing GFP alone showed no significant changes in gridness score or firing rates compared to baseline (Figure S2).

Modulation of MS-GABAergic activity disrupts GC temporal coding

As MS-GABAergic neurons contribute to ongoing theta oscillations in the MEC, periodic disruptions to rhythmic theta inputs to entorhinal interneurons may alter GC temporal coding in the form of impaired theta phase precession. Oscillatory interference and continuous attractor network models suggest that theta phase precession could allow GCs to integrate spatial displacement based on self-motion while planning future paths as part of a path integration system.[30–32] Previous literature has shown that driving endogenous theta above the theta range results in a disruption in GC theta phase precession.[24] To examine whether theta phase precession is affected in GCs during periodic optogenetic ihb, we computed the strength of correlation between the distance traveled across a grid field and the theta phase of spiking (Figures 2D and 2E). We observed that, of seven GCs that exhibited phase precession during baseline recordings, six no longer showed phase precession when theta power was periodically disrupted during the 30-s ihb with 30-s ISI recording sessions (Figure 2D). We further examined whether phase precession returned during the 30-s ISI periods and observed the same finding, that 6 of 7 GCs exhibited no phase precession even with the return of theta oscillations (Figure 2D). Interestingly, while the correlation between the spiking phase and distance traveled across a firing field phase precession was disrupted significantly, phase precession slopes remained negative in all except one neuron (Figure 2F). It has been shown previously that GC periodicity and phase precession are dissociable, our data support these findings, with cells that cease to phase precess showing variability in their grid scores with ihb (Figure 2G). Our results suggest that intermittent silencing of MS-GABAergic cells can disrupt the integration of self-motion-based cues via theta phase precession.

Given that grid spatial firing was disrupted during the 30-s ihb period as well as the 30-s ISI period, we examined whether extending the duration of the ISI period would allow for recovery of GC spatial firing. For this, we used a 30-s ihb period followed by a 60-s ISI period repeated throughout the entire recording session. The 30-s ihb period results in a large decrease in theta power, with a return of power following the ihb period (Figures 3A and 3B). In these experiments, we tracked neurons across three recordings: baseline, 30-s ihb with 30-s ISI protocol, and 30-s ihb with 60-s ISI periods. Tracking the same cells with different interstimulus lengths revealed that the longer ISI period of 60 s between ihb periods allowed for the recovery of the GC spatial firing pattern (Figures 3A and 3B; $n = 8$ GCs, mean ± SEM, baseline mean 0.52 ± 0.12, 30-s ihb + 30-s ISI 0.0036 ± 0.14, 30-s ihb + 60-s ISI = 0.4352 ± 0.223, Friedman test $p < 0.05$ with Dunn's multiple-comparisons, test baseline vs. 30-s ihb + 30-s ISI $p < 0.05$, baseline vs. 30-s ihb + 60-s ISI, $p = 0.6346$). Next, we examined the time course of GC disruption and recovery by calculating gridness scores in 30-s intervals via a rolling window analysis (Figures 3D and 3E; STAR Methods). When normalized against baseline gridness scores, GC periodicity was disrupted as early as 9–39 s following laser onset ($n = 9$ GCs, mean ± SEM; normalized gridness score 0.4376 ± 0.2086, one sample Wilcoxon test; $p < 0.05$), reached its lowest points between 39 and 69 s (−0.009709 ± 0.3310, $p < 0.05$) and 51–81 s following laser onset (0.3373 ± 0.1930, $p < 0.01$) and recovered at 60–90 s following laser onset (0.6219 ± 0.1775, $p = 0.0977$). Theta power shows disruption during laser-on with more rapid recovery in laser-off periods (Figure 3C). These data reveal that disruption of MS-GABAergic input and the reduction of ongoing MEC theta oscillations results in the rapid degradation of GC

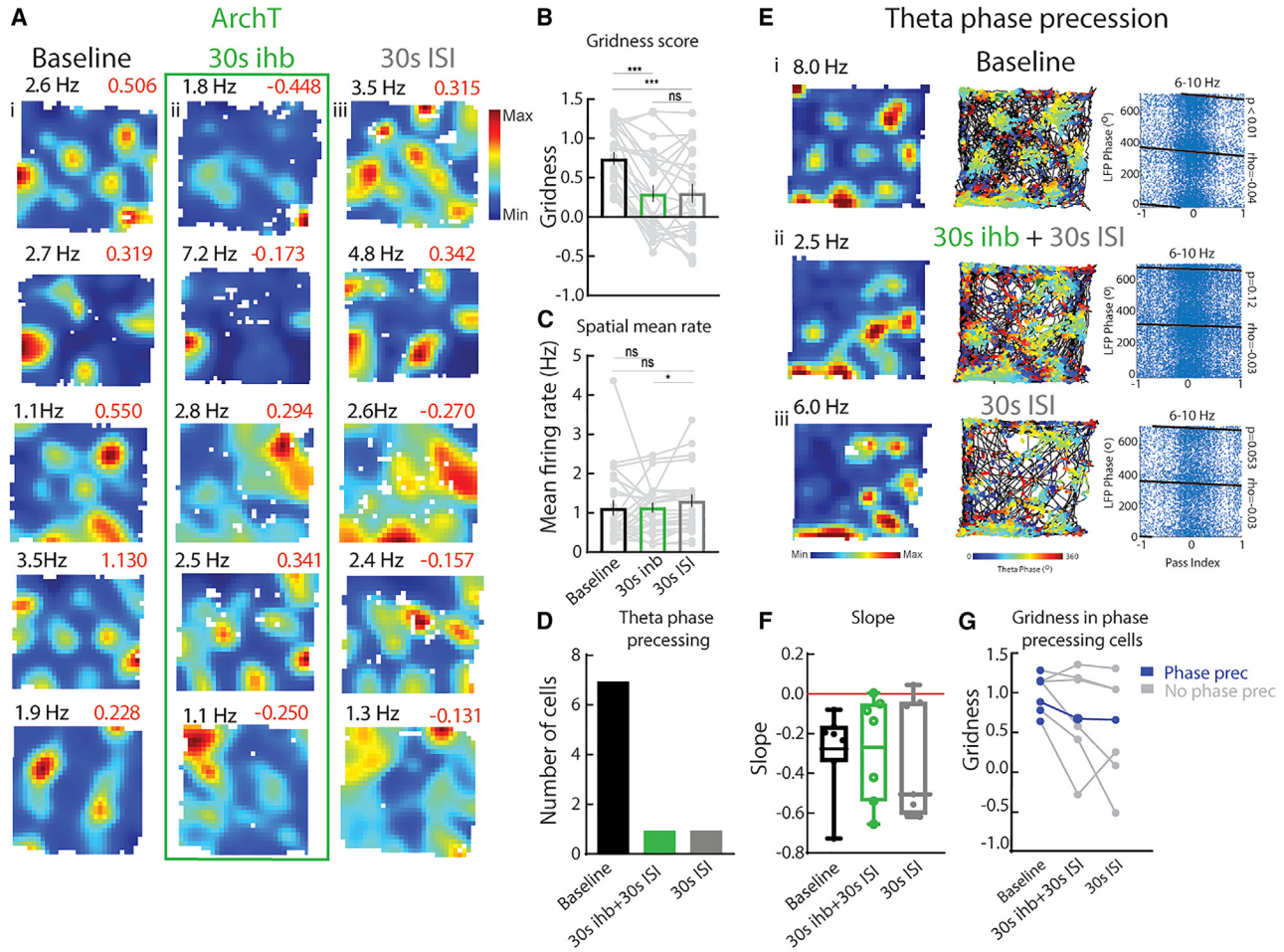

Figure 2. Optogenetic MS GABAergic ihb disrupts GC spatial periodicity and phase precession during both 30-s ihb and 30-s ISI

(A) Example rate maps of GCs in (i) baseline and separated into (ii) 30-s ihb and (iii) 30-s ISI conditions, with peak firing rate shown in black and gridness score in red above each rate map.

(B) Gridness score across baseline, 30-s ihb periods, and 30-s ISI periods (n = 25 cells, Friedman test with Dunn's multiple-comparisons test, $p < 0.001$).

(C) Mean firing rate (Hz) across baseline, 30-s ihb periods, and 30-s ISI periods (n = 25 cells, Friedman test with Dunn's multiple-comparisons test, $p < 0.05$).

(D) Number of cells phase precessing during baseline and 30-s laser-on and 30-s laser-off stimulations. We observed one neuron that continued to phase precess during the stimulation ($p < 0.01$).

(E) Analysis of 2D precession data, including a rate map (left), trajectory plot (center), and phase of spiking. Pass index values of −1 and +1 represent the entry and exit of a firing field. The regression line on the right indicates that the spike phase predicts the position of the animal within the field. The p value of phase precession is shown on the right. The example unit ceased phase precessing during stimulation, as shown by the loss of significant phase precession that initially appears in the top plot ($p < 0.01$).

(F) Phase precession slopes for baseline, 30-s ihb + 30-s ISI and 30-s ISI-only periods (n = 7 cells; median ± IQR, baseline −0.2023 ± 0.1767, 30-s ihb + 30-s ISI −0.1359 ± 0.490, 30-s ISI −0.5058 ± 0.5620).

(G) Change in grid score from baseline with 30-s ihb + 30-s ISI and 30-s ISI periods, with color indicating phase-precessing cells.

*$p < 0.05$, ***$p < 0.001$. Unless indicated otherwise, all results are presented as mean ± SEM.

periodicity over a time course similar to that observed in the absence of visual input[4] and that the GC network requires up to 30–60 s to regain stable spatial firing.

DISCUSSION

Our research supports the theory that the spatial firing patterns of entorhinal GCs are dependent on theta oscillations and underscores the critical role of the MS-GABAergic neurons for GC spatial and temporal coding. The data show loss of GC spatial periodicity during inactivation of MS-GABAergic neurons. Furthermore, these data demonstrate that GC spatial firing does not recover with the same time course as theta oscillations. When optogenetic ihb of MS-GABAergic cells was terminated, theta oscillations returned immediately, however GC spatial firing was not restored within a 30-s ISI period. Additional experiments show that a longer recovery interval of 60 s facilitates the restoration of GC spatial firing. Our findings provide support to theoretical models of GCs where a disruption in representation would take time to recover to a stable attractor space.

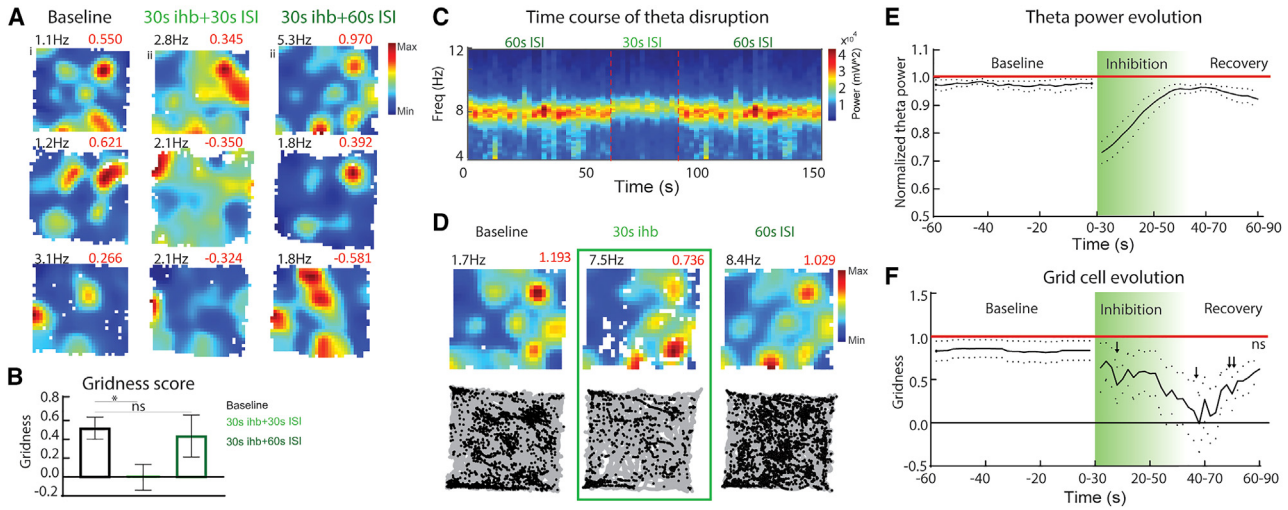

Figure 3. Increasing ISIs resulted in GC spatial periodicity recovery

(A) Example rate maps for cells recorded across (i) baseline, (ii) combined 30-s silencing followed by 30-s ISI, and (iii) 30-s silencing periods followed by 60-s ISI stimulation. Peak firing rate is shown in black and gridness score in red above each rate map.

(B) Grid score for baseline, combined 30-s silencing and 30-s ISI, and combined 30-s silencing and 60-s ISI (n = 8 cells, Friedman test with Dunn's multiple-comparisons test, $p < 0.05$).

(C) Example power spectrogram of LFP power averaged across the entire recording session. Note that the two 60-s ISI examples are the same data represented twice.

(D) Example rate map and trajectory (with spiking locations in black) of baseline and separated rate maps for the 30-s silencing period and 60-s ISI periods. Peak firing rate is shown in black and gridness score in red above each rate map.

(E) Example theta power evolution calculated using a 30-s rolling window following stimulation onset normalized to max theta power (n = 23 stimulations from 1 recording session).

(F) Gridness evolution calculated by a 30-s rolling window beginning 1 s following stimulation onset, normalized to shuffled baseline (n = 9 cells, one-sample Wilcoxon test; $p < 0.05$, $p < 0.01$).

*$p < 0.05$, → $p < 0.05$, →→ $p < 0.01$. Unless indicated otherwise, all results are presented as mean ± SEM.

Our findings contrast with recent reports that observed no alteration in GC spatial periodicity when MS-GABAergic neurons were stimulated to drive MEC oscillations beyond the endogenous theta frequency range.[24,27] Our results are more similar to MS pharmacological inactivation experiments that result in disruptions to GC spatial periodicity.[9,10] This discrepancy suggests that GCs require a consistent rhythmic network activity to maintain spatial periodicity but may not require a specific frequency.

We demonstrate that MS-GABAergic ihb also reduced temporal coding by GCs, evidenced by attenuation of phase precession. In the hippocampus, septal inactivation or MS-GABAergic driving results in a variable response, with some but not all place cells ceasing to precess.[23,33] In comparison, stimulation of MS PV+ GABAergic neurons above the theta range disrupted phase precession in all GCs in the MEC,[24] while activation of MS calbindin-positive axons in the MEC enhanced phase precession.[34] In our experiments, theta disruption attenuated phase precession across the entire recording, including when optogenetic inactivation was released and theta oscillations returned. This indicates that theta oscillations themselves are not sufficient for phase precession to occur and that ample recovery time is critical for both GCs' spatial and temporal coding. Although previous research has shown that the spatial and temporal firing patterns of GCs are dissociable,[24] our data demonstrate that the spatial and temporal dynamics of GC activity are interconnected and dependent on both MS-GABAergic neuron activity and the presence of theta oscillations.

In the MS, GABAergic cell types express H current that contributes to the generation of rhythmic activity in slice preparations[35,36] and in behaving animals.[17,37,38] This rhythmicity likely plays a role in the periodic ihb of local interneurons in superficial layers of the MEC,[20,34] thereby disinhibiting the circuit in a manner similar to the pacing of theta rhythm in the hippocampus.[19,39] Many recent studies suggest that PV+ MS neurons are responsible for pacing theta oscillations in the MEC.[24,27,40–42] The MS-GABAergic population is heterogeneous in terms of subpopulation, neurochemical marker expression, and targeting area.[43] Within the PV+ population of MS-GABAergic neurons, PV+ neurons that project to the superficial layers of the MEC preferably fire at the peak of theta, while hippocampus-targeting PV+ MS GABAergic neurons fire at the trough.[44] While the effects shown here on both theta oscillations and GC coding may be due to direct projections to layers II–III of the MEC, it is also possible that the disruption of GC spatial and temporal coding is due to an interruption of hippocampal inputs. MS-GABAergic neurons project both to the MEC and hippocampal interneurons,[19,20] and although we did not record in the hippocampus, we posit that theta oscillations were also disrupted in the hippocampus as well. It has been shown previously that pharmacological inactivation of the hippocampus results in a reduction of the grid spatial firing in the MEC.[8] Given that we targeted all GABAergic neurons in the MS, we cannot distinguish between

the effect on direct projections to the MEC and indirect effects causing the disruption in spatial periodicity.

One major advantage of using optogenetic modulation rather than pharmacological or chemogenetic modulation is the rapid decrease and recovery of theta oscillations following ihb. Our data show that, while optogenetic ihb results in an instantaneous disruption of theta oscillations, it does not immediately degrade GC periodicity, but, rather, the gridness score takes up to ~10–40 s to devolve. These data are similar to the time course of disruption of GC firing observed when there was an abrupt absence of visual input (darkness) in which disruptions of GC spatial firing were observed in the first 30 s.[4] Though the underlying mechanisms of GC disruption are distinct, both show that, with a lack of specific inputs, whether it be visual or oscillatory, the GC network devolves relatively quickly. In contrast to visual landmarks, the GC firing pattern takes much longer to recover from theta disruptions. While GC stability returns in the first 10 s after transitioning from darkness to the light condition,[4] our study revealed that, following 30 s of theta disruption, the GC network required 60–90 s to return to spatial firing. This phenomenon provides insight into GC network dynamics and highlights the important role of MS-GABAergic inputs and theta oscillations.

The MS contributes to spatial memory, as demonstrated by lesion and inactivation experiments.[12,14,45] Similarly, selective inactivation of MS-GABAergic neurons results in impaired spatial memory.[34,46,47] Our study suggests that the activity of MS-GABAergic neurons is essential to the spatial firing of the GC network, thus contributing to the formation of an internal spatial map of the external world necessary for spatial memory. Together, these data point to MS-GABAergic neurons and GC disruption as a potential mechanism underlying the spatial navigation and memory deficits related to MS dysfunction.

Limitations of the study

In our study, we examine how silencing MS-GABAergic neurons affects GC coding. Since our study is focused on just one MS cell type, the role of MS glutamatergic or cholinergic neurons in GC spatial or temporal coding remains unclear. Previous studies have shown that chemogenetic activation of MS-cholinergic neurons has no effect on grid coding[48] and that MS-glutamatergic neurons project to the MEC.[49] However, it has yet to be reported whether silencing either population affects GC coding. Future work will need to target each of the remaining MS populations to examine whether any of these neurons play a role in GC spatial or temporal coding in the MEC.

In the current study, both male and female mice were implanted and recorded, but due to the weight of the implant and tether, female mice had very poor trajectories, and therefore only data from male mice could be included in the present dataset. While prior studies have not revealed sex differences in the physiological phenomena addressed in this study, the exclusion of female mice represents a limitation to the interpretation of the results.

As discussed above, the MS-GABAergic population has heterogeneous subpopulations with distinct neurochemical markers and targeted areas within the hippocampal-entorhinal network. The current study examines the entire MS-GABAergic population; however, the diverse projection patterns of this population limit the interpretation of the results. Future work could aim to unpack each MS-GABAergic subpopulation using several separate mouse lines or examine whether the effects observed in the current study are due to direct or indirect projections from the MS to the MEC using retrograde optogenetic tools. These experiments may provide further insight into the relationship between the MS, hippocampus, and MEC in GC spatial and temporal coding.

STAR★METHODS

Detailed methods are provided in the online version of this paper and include the following:

- KEY RESOURCES TABLE
- RESOURCE AVAILABILITY
  - Lead contact
  - Materials availability
  - Data and code availability
- EXPERIMENTAL MODEL AND STUDY PARTICIPANT DETAILS
  - Mice
- METHOD DETAILS
  - Surgeries
  - Data acquisition
  - Optogenetic experiments
  - Histology
  - Data processing
- QUANTIFICATION AND STATISTICAL ANALYSIS
  - Data analysis
  - Measurement of single unit properties
  - Statistics

SUPPLEMENTAL INFORMATION

Supplemental information can be found online at https://doi.org/10.1016/j.celrep.2024.114590.

ACKNOWLEDGMENTS

We would like to thank P. Mannarin and S. Kim for technical assistance with this project. We are also grateful to J.Q. Lee and M. Yaghoubi, who provided comments on prior versions of the manuscript, and to all members of the Hasselmo and Brandon laboratories for helpful discussions and advice on this project. Funding was provided by Canadian Institutes of Health Research grants 367017 and 377074 (to M.P.B.), Natural Sciences and Engineering Research Council of Canada grant 74105 (to M.P.B.), National Institute of Mental Health grant R01 MH120073 (to M.E.H.), and Office of Naval Research grant MURI N00014-19-1-2571 (to M.E.H.).

AUTHOR CONTRIBUTIONS

J.C.R., M.E.H., and M.P.B. designed the research study. J.C.R. performed experiments. J.C.R. and J.Y. analyzed data. J.C.R., M.E.H., and M.P.B. wrote the paper.

DECLARATION OF INTERESTS

The authors declare no competing interests.

Received: February 8, 2024
Revised: May 29, 2024
Accepted: July 21, 2024
Published: August 19, 2024

REFERENCES

1. Hafting, T., Fyhn, M., Molden, S., Moser, M.B., and Moser, E.I. (2005). Microstructure of a spatial map in the entorhinal cortex. Nature *436*, 801–806. https://doi.org/10.1038/nature03721.
2. Fyhn, M., Molden, S., Witter, M.P., Moser, E.I., and Moser, M.B. (2004). Spatial representation in the entorhinal cortex. Science *305*, 1258–1264. https://doi.org/10.1126/science.1099901.
3. Moser, E.I., Kropff, E., and Moser, M.B. (2008). Place cells, grid cells, and the brain's spatial representation system. Annu. Rev. Neurosci. *31*, 69–89. https://doi.org/10.1146/annurev.neuro.31.061307.090723.
4. Perez-Escobar, J.A., Kornienko, O., Latuske, P., Kohler, L., and Allen, K. (2016). Visual landmarks sharpen grid cell metric and confer context specificity to neurons of the medial entorhinal cortex. Elife *5*, e16937. https://doi.org/10.7554/eLife.16937.
5. Sargolini, F., Fyhn, M., Hafting, T., McNaughton, B.L., Witter, M.P., Moser, M.B., and Moser, E.I. (2006). Conjunctive representation of position, direction, and velocity in entorhinal cortex. Science *312*, 758–762. https://doi.org/10.1126/science.1125572.
6. Campbell, M.G., and Giocomo, L.M. (2018). Self-motion processing in visual and entorhinal cortices: inputs, integration, and implications for position coding. J. Neurophysiol. *120*, 2091–2106. https://doi.org/10.1152/jn.00686.2017.
7. Winter, S.S., Clark, B.J., and Taube, J.S. (2015). Spatial navigation. Disruption of the head direction cell network impairs the parahippocampal grid cell signal. Science *347*, 870–874. https://doi.org/10.1126/science.1259591.
8. Bonnevie, T., Dunn, B., Fyhn, M., Hafting, T., Derdikman, D., Kubie, J.L., Roudi, Y., Moser, E.I., and Moser, M.B. (2013). Grid cells require excitatory drive from the hippocampus. Nat. Neurosci. *16*, 309–317. https://doi.org/10.1038/nn.3311.
9. Brandon, M.P., Bogaard, A.R., Libby, C.P., Connerney, M.A., Gupta, K., and Hasselmo, M.E. (2011). Reduction of theta rhythm dissociates grid cell spatial periodicity from directional tuning. Science *332*, 595–599. https://doi.org/10.1126/science.1201652.
10. Koenig, J., Linder, A.N., Leutgeb, J.K., and Leutgeb, S. (2011). The spatial periodicity of grid cells is not sustained during reduced theta oscillations. Science *332*, 592–595. https://doi.org/10.1126/science.1201685.
11. Jeffery, K.J., Donnett, J.G., and O'Keefe, J. (1995). Medial septal control of theta-correlated unit firing in the entorhinal cortex of awake rats. Neuroreport *6*, 2166–2170. https://doi.org/10.1097/00001756-199511000-00017.
12. Mitchell, S.J., Rawlins, J.N., Steward, O., and Olton, D.S. (1982). Medial septal area lesions disrupt theta rhythm and cholinergic staining in medial entorhinal cortex and produce impaired radial arm maze behavior in rats. J. Neurosci. *2*, 292–302. https://doi.org/10.1523/JNEUROSCI.02-03-00292.1982.
13. Mizumori, S.J., Perez, G.M., Alvarado, M.C., Barnes, C.A., and McNaughton, B.L. (1990). Reversible inactivation of the medial septum differentially affects two forms of learning in rats. Brain Res. *528*, 12–20. https://doi.org/10.1016/0006-8993(90)90188-h.
14. Winson, J. (1978). Loss of hippocampal theta rhythm results in spatial memory deficit in the rat. Science *201*, 160–163. https://doi.org/10.1126/science.663646.
15. Chrobak, J.J., Stackman, R.W., and Walsh, T.J. (1989). Intraseptal administration of muscimol produces dose-dependent memory impairments in the rat. Behav. Neural. Biol. *52*, 357–369. https://doi.org/10.1016/s0163-1047(89)90472-x.
16. Colom, L.V., Castaneda, M.T., Reyna, T., Hernandez, S., and Garrido-Sanabria, E. (2005). Characterization of medial septal glutamatergic neurons and their projection to the hippocampus. Synapse *58*, 151–164. https://doi.org/10.1002/syn.20184.
17. Simon, A.P., Poindessous-Jazat, F., Dutar, P., Epelbaum, J., and Bassant, M.H. (2006). Firing properties of anatomically identified neurons in the medial septum of anesthetized and unanesthetized restrained rats. J. Neurosci. *26*, 9038–9046. https://doi.org/10.1523/JNEUROSCI.1401-06.2006.
18. Hangya, B., Borhegyi, Z., Szilágyi, N., Freund, T.F., and Varga, V. (2009). GABAergic neurons of the medial septum lead the hippocampal network during theta activity. J. Neurosci. *29*, 8094–8102. https://doi.org/10.1523/JNEUROSCI.5665-08.2009.
19. Freund, T.F., and Antal, M. (1988). GABA-containing neurons in the septum control inhibitory interneurons in the hippocampus. Nature *336*, 170–173. https://doi.org/10.1038/336170a0.
20. Gonzalez-Sulser, A., Parthier, D., Candela, A., McClure, C., Pastoll, H., Garden, D., Sürmeli, G., and Nolan, M.F. (2014). GABAergic projections from the medial septum selectively inhibit interneurons in the medial entorhinal cortex. J. Neurosci. *34*, 16739–16743. https://doi.org/10.1523/JNEUROSCI.1612-14.2014.
21. Amilhon, B., Huh, C.Y.L., Manseau, F., Ducharme, G., Nichol, H., Adamantidis, A., and Williams, S. (2015). Parvalbumin Interneurons of Hippocampus Tune Population Activity at Theta Frequency. Neuron *86*, 1277–1289. https://doi.org/10.1016/j.neuron.2015.05.027.
22. Dannenberg, H., Pabst, M., Braganza, O., Schoch, S., Niediek, J., Bayraktar, M., Mormann, F., and Beck, H. (2015). Synergy of direct and indirect cholinergic septo-hippocampal pathways coordinates firing in hippocampal networks. J. Neurosci. *35*, 8394–8410. https://doi.org/10.1523/JNEUROSCI.4460-14.2015.
23. Zutshi, I., Brandon, M.P., Fu, M.L., Donegan, M.L., Leutgeb, J.K., and Leutgeb, S. (2018). Hippocampal Neural Circuits Respond to Optogenetic Pacing of Theta Frequencies by Generating Accelerated Oscillation Frequencies. Curr. Biol. *28*, 1179–1188.e3. https://doi.org/10.1016/j.cub.2018.02.061.
24. Lepperod, M.E., Christensen, A.C., Lensjo, K.K., Buccino, A.P., Yu, J., Fyhn, M., and Hafting, T. (2021). Optogenetic pacing of medial septum parvalbumin-positive cells disrupts temporal but not spatial firing in grid cells. Sci. Adv. *7*, eabd5684. https://doi.org/10.1126/sciadv.abd5684.
25. Boyce, R., Glasgow, S.D., Williams, S., and Adamantidis, A. (2016). Causal evidence for the role of REM sleep theta rhythm in contextual memory consolidation. Science *352*, 812–816. https://doi.org/10.1126/science.aad5252.
26. Dannenberg, H., Kelley, C., Hoyland, A., Monaghan, C.K., and Hasselmo, M.E. (2019). The Firing Rate Speed Code of Entorhinal Speed Cells Differs across Behaviorally Relevant Time Scales and Does Not Depend on Medial Septum Inputs. J. Neurosci. *39*, 3434–3453. https://doi.org/10.1523/JNEUROSCI.1450-18.2019.
27. Quirk, C.R., Zutshi, I., Srikanth, S., Fu, M.L., Devico Marciano, N., Wright, M.K., Parsey, D.F., Liu, S., Siretskiy, R.E., Huynh, T.L., et al. (2021). Precisely timed theta oscillations are selectively required during the encoding phase of memory. Nat. Neurosci. *24*, 1614–1627. https://doi.org/10.1038/s41593-021-00919-0.
28. Han, X., Chow, B.Y., Zhou, H., Klapoetke, N.C., Chuong, A., Rajimehr, R., Yang, A., Baratta, M.V., Winkle, J., Desimone, R., and Boyden, E.S. (2011). A high-light sensitivity optical neural silencer: development and application to optogenetic control of non-human primate cortex. Front. Syst. Neurosci. *5*, 18. https://doi.org/10.3389/fnsys.2011.00018.
29. Yartsev, M.M., Witter, M.P., and Ulanovsky, N. (2011). Grid cells without theta oscillations in the entorhinal cortex of bats. Nature *479*, 103–107. https://doi.org/10.1038/nature10583.
30. Burgess, N., Barry, C., and O'Keefe, J. (2007). An oscillatory interference model of grid cell firing. Hippocampus *17*, 801–812. https://doi.org/10.1002/hipo.20327.
31. Burgess, N. (2008). Grid cells and theta as oscillatory interference: theory and predictions. Hippocampus *18*, 1157–1174. https://doi.org/10.1002/hipo.20518.
32. Navratilova, Z., Giocomo, L.M., Fellous, J.M., Hasselmo, M.E., and McNaughton, B.L. (2012). Phase precession and variable spatial scaling

in a periodic attractor map model of medial entorhinal grid cells with realistic after-spike dynamics. Hippocampus *22*, 772–789. https://doi.org/10.1002/hipo.20939.

33. Schlesiger, M.I., Cannova, C.C., Boublil, B.L., Hales, J.B., Mankin, E.A., Brandon, M.P., Leutgeb, J.K., Leibold, C., and Leutgeb, S. (2015). The medial entorhinal cortex is necessary for temporal organization of hippocampal neuronal activity. Nat. Neurosci. *18*, 1123–1132. https://doi.org/10.1038/nn.4056.
34. Schlesiger, M.I., Ruff, T., MacLaren, D.A.A., Barriuso-Ortega, I., Saidov, K.M., Yen, T.Y., and Monyer, H. (2021). Two septal-entorhinal GABAergic projections differentially control coding properties of spatially tuned neurons in the medial entorhinal cortex. Cell Rep. *34*, 108801. https://doi.org/10.1016/j.celrep.2021.108801.
35. Serafin, M., Williams, S., Khateb, A., Fort, P., and Mühlethaler, M. (1996). Rhythmic firing of medial septum non-cholinergic neurons. Neuroscience *75*, 671–675. https://doi.org/10.1016/0306-4522(96)00349-1.
36. Griffith, W.H. (1988). Membrane properties of cell types within guinea pig basal forebrain nuclei in vitro. J. Neurophysiol. *59*, 1590–1612. https://doi.org/10.1152/jn.1988.59.5.1590.
37. Xu, C., Datta, S., Wu, M., and Alreja, M. (2004). Hippocampal theta rhythm is reduced by suppression of the H-current in septohippocampal GABAergic neurons. Eur. J. Neurosci. *19*, 2299–2309. https://doi.org/10.1111/j.0953-816X.2004.03316.x.
38. Varga, V., Hangya, B., Kránitz, K., Ludányi, A., Zemankovics, R., Katona, I., Shigemoto, R., Freund, T.F., and Borhegyi, Z. (2008). The presence of pacemaker HCN channels identifies theta rhythmic GABAergic neurons in the medial septum. J. Physiol. *586*, 3893–3915. https://doi.org/10.1113/jphysiol.2008.155242.
39. Toth, K., Freund, T.F., and Miles, R. (1997). Disinhibition of rat hippocampal pyramidal cells by GABAergic afferents from the septum. J Physiol *500*, 463–474. https://doi.org/10.1113/jphysiol.1997.sp022033.
40. Etter, G., van der Veldt, S., Choi, J., and Williams, S. (2023). Optogenetic frequency scrambling of hippocampal theta oscillations dissociates working memory retrieval from hippocampal spatiotemporal codes. Nat. Commun. *14*, 410. https://doi.org/10.1038/s41467-023-35825-5.
41. Bender, F., Gorbati, M., Cadavieco, M.C., Denisova, N., Gao, X., Holman, C., Korotkova, T., and Ponomarenko, A. (2015). Theta oscillations regulate the speed of locomotion via a hippocampus to lateral septum pathway. Nat. Commun. *6*, 8521. https://doi.org/10.1038/ncomms9521.
42. Robinson, J.C., Wilmot, J.H., and Hasselmo, M.E. (2023). Septo-hippocampal dynamics and the encoding of space and time. Trends Neurosci. *46*, 712–725. https://doi.org/10.1016/j.tins.2023.06.004.
43. Fuchs, E.C., Neitz, A., Pinna, R., Melzer, S., Caputi, A., and Monyer, H. (2016). Local and Distant Input Controlling Excitation in Layer II of the Medial Entorhinal Cortex. Neuron *89*, 194–208. https://doi.org/10.1016/j.neuron.2015.11.029.
44. Viney, T.J., Salib, M., Joshi, A., Unal, G., Berry, N., and Somogyi, P. (2018). Shared rhythmic subcortical GABAergic input to the entorhinal cortex and presubiculum. Elife *7*, e34395. https://doi.org/10.7554/eLife.34395.
45. Mizumori, S.J., Barnes, C.A., and McNaughton, B.L. (1990). Behavioral correlates of theta-on and theta-off cells recorded from hippocampal formation of mature young and aged rats. Exp. Brain Res. *80*, 365–373. https://doi.org/10.1007/BF00228163.
46. Pang, K.C.H., Jiao, X., Sinha, S., Beck, K.D., and Servatius, R.J. (2011). Damage of GABAergic neurons in the medial septum impairs spatial working memory and extinction of active avoidance: effects on proactive interference. Hippocampus *21*, 835–846. https://doi.org/10.1002/hipo.20799.
47. Roland, J.J., Stewart, A.L., Janke, K.L., Gielow, M.R., Kostek, J.A., Savage, L.M., Servatius, R.J., and Pang, K.C.H. (2014). Medial septum-diagonal band of Broca (MSDB) GABAergic regulation of hippocampal acetylcholine efflux is dependent on cognitive demands. J. Neurosci. *34*, 506–514. https://doi.org/10.1523/JNEUROSCI.2352-13.2014.
48. Carpenter, F., Burgess, N., and Barry, C. (2017). Modulating medial septal cholinergic activity reduces medial entorhinal theta frequency without affecting speed or grid coding. Sci. Rep. *7*, 14573. https://doi.org/10.1038/s41598-017-15100-6.
49. Justus, D., Dalügge, D., Bothe, S., Fuhrmann, F., Hannes, C., Kaneko, H., Friedrichs, D., Sosulina, L., Schwarz, I., Elliott, D.A., et al. (2017). Glutamatergic synaptic integration of locomotion speed via septoentorhinal projections. Nat. Neurosci. *20*, 16–19. https://doi.org/10.1038/nn.4447.
50. Schneider, C.A., Rasband, W.S., and Eliceiri, K.W. (2012). NIH Image to ImageJ: 25 years of image analysis. Nat. Methods *9*, 671–675. https://doi.org/10.1038/nmeth.2089.
51. Mitra, P.P., and Bokil, H. (2007). Observed Brain Dynamics (Oxford University Press).
52. Dannenberg, H., Lazaro, H., Nambiar, P., Hoyland, A., and Hasselmo, M.E. (2020). Effects of visual inputs on neural dynamics for coding of location and running speed in medial entorhinal cortex. Elife. *9*, e62500. https://doi.org/10.7554/eLife.62500.
53. Climer, J.R., Newman, E.L., and Hasselmo, M.E. (2013). Phase coding by grid cells in unconstrained environments: two-dimensional phase precession. Eur. J. Neurosci. *38*, 2526–2541.

STAR★METHODS

KEY RESOURCES TABLE

REAGENT or RESOURCE	SOURCE	IDENTIFIER
Antibodies		
Alexa Fluor 488	Abcam	Cat A-21206: RRID:AB_2535792
GFP rabbit antiserum	Invitrogen	Cat A-11122: RRID:AB_221569
Bacterial and virus strains		
AAVdj-EF1α-Flex-ArchT-GFP	University of North Carolina Virus Core & NeuroPhotonics Center	https://www.med.unc.edu/genetherapy/vectorcore/in-stock-aav-vectors/boyden/ & https://neurophotonics.ca/list-available-molecular-tools/
AAV2/2-Syn-GFP	NeuroPhotonics Center	https://neurophotonics.ca/list-available-molecular-tools/
Experimental models: Organisms/strains		
Mice/VGAT^{Cre} knock-in homozygote mice	The Jackson Laboratory	stock # 016962 stock # 028862
Software and algorithms		
MATLAB 2020a	MatWorks	https://www.mathworks.com/products/matlab.html
Offline Sorter	Plexon	https://plexon.com/products/offline-sorter/
Chronux toolbox	Mitra lab	http://chronux.org/
Custom MATLAB scripts	Hasselmo/Brandon labs	https://doi.org/10.5281/zenodo.12738560
Prism 9	Graphpad	https://www.graphpad.com/features
ImageJ	Schneider et al.[50]	https://imagej.nih.gov/ij/
Zeiss AxioImager	Zeiss	N/A
Other		
Optic fiber	Thorlabs	CF230
Ferrule	Precision Fiber Products	MM-FER2007C
530 nm laser	Doric Lenses	LDFLS_520/060

RESOURCE AVAILABILITY

Lead contact

Further information and requests for resources should be directed to and will be fulfilled by the lead contact, Jennifer C. Robinson (jenniferclaire.robinson@gmail.com).

Materials availability

This study did not generate any new reagents.

Data and code availability

- Datasets supporting the current study will be shared by the lead contact upon request.
- Original code has been deposited at Zenodo (https://doi.org/10.5281/zenodo.12738559).
- Any additional information required to reanalyze the data reported in this paper is available from the lead contact upon request.

EXPERIMENTAL MODEL AND STUDY PARTICIPANT DETAILS

Mice

All procedures were performed according to protocols and guidelines approved by the Institutional Animal Care and Use Committee at Boston University and the McGill University Animal Care Committee and the Canadian Council on Animal Care. VGAT^{Cre} knock-in homozygote mice (The Jackson Laboratory, stock # 016962) were housed in a 12:12 h light/dark cycle with food and water *ad libitum*.

The housing room conditions of the mice were maintained at 20–22°C and 21–30% humidity. Specificity of this mouse line for Cre recombinase has previously been confirmed in this mouse line (Boyce et al., 2016).

METHOD DETAILS

Surgeries

For all surgeries, mice were anesthetized via oxygen and 5% isoflurane in an inhalation box and then transferred to the stereotaxic frame (David Kopf Instruments), where anesthesia was maintained via inhalation of oxygen and 1–2.5% isoflurane for the duration of the surgery. The animals' body temperature was maintained via heating pad and eyes were protected with hydrogel (Optixcare). The anesthetic Carprofen was administered subcutaneously during each surgery.

To drive the expression of the opsins, 10–14 week old VGAT-Cre mice were stereotaxically injected in the MS with a Cre-dependent adeno-associated viral vectors. Silencing experiments were performed with ArchT-GFP (AAVdj-EF1α-Flex-ArchT-GFP from University of North Carolina Virus Core) and virus control experiments were performed with GFP (AAV2-*syn*-GFP from). Viruses were delivered directly into the medial septum at AP 0.86 mm from bregma, ML 0.0 mm, DV 4.5–4.7mm. All injections were administered via glass pipettes connected to a Nanoject II (Drummond Scientific) injector at a flow rate of 23 nL/s.

Following a 2–4 week incubation period, mice underwent a second surgery to implant an optic fiber and microdrive. For each mouse, two stainless anchor screws (B000FN0J58, Antrin Online) were placed in front of the inferior cerebral vein, and were secured to the skull with dental cement (Patterson Dental, Inc). A ground wire was positioned above the contralateral cerebellum. For optogenetic modulation of the medial septum an optic fiber (CF230, Thorlabs) connected to a ferrule (Precision Fiber Products or Thorlabs) was implanted at a 5° angle to target just above the medial septum (AP 0.86, ML 0.2, DV 3.83 mm) and secured to the skull with dental cement. Electrophysiological experiments were performed with custom made microdrives. The microdrive used consisted of four independently movable tetrodes (Axona, Inc) and was implanted above of the MEC at the following stereotaxic coordinates: 3.4 mm lateral to the midline, 0.25–0.40 mm anterior to the transverse sinus at an 8–10°angle. Tetrodes were gold-plated using the NanoZ (Neuralynx) to lower impedances to 200–250 kΩ at 1 kHz and dipped in mineral oil prior to surgery. The microdrive was secured in place with metabond and dental cement (Patterson Dental). Once the cement was dry, tetrodes were lowered 400um below the surface of the brain. Mouse body temperature was maintained using a heating pad throughout the surgery until fully recovered. Both male and female mice were implanted however due to the weight of the implant and tether, female mice produced very poor trajectories and only data from male mice are included in the present dataset.

Data acquisition

Following surgery, animals had 1 week of recovery. Once recovered, mice were placed on water restriction and maintained at 85% of their *ad libidum* weight for the duration of experiments. Animals were connected to custom-built headstage preamplifier tethers (Neuralynx) and an optic fiber patch cord (Thorlabs). Light delivery was achieved through an optic fiber patch cord and sleeve coupled to a 530 nm laser (Doric), and light intensity was set for 20 mW. Neural recordings were amplified and band-pass filtered between 0.6 kHz and 6 kHz using a Digital Lynx SX recording system (Neuralynx) and stored with Cheetah Software (Neuralynx). Animals were recorded in an open field (75 × 75 cm square box). Tetrodes were advanced at 25 μm increments to sample neurons. Spike waveform thresholds were adjusted before commencing each recording and ranged between 25 and 140 μV depending on unit activity. Waveforms that crossed threshold were digitized at 32 kHz and recorded across all four channels of the given tetrode. Local field potentials were recorded across all tetrodes.

Optogenetic experiments

During recording, the environment was dimly lit and white-noise was played to mask uncontrolled ambient sounds. Following each recording the environment was cleaned with disinfectant (Prevail). Once grid cells had been identified during a baseline recording, light delivery was achieved through an optic fiber patch cord and sleeve coupled to a green laser (520nm wavelength, maximum power output: 60mW, Doric Lenses) and light intensity at the tip of the optic fiber was estimated for between 15 and 20 mW. Stimulation protocols consisted of 30s laser-on periods followed by 30s laser-off periods throughout the entire experimental recording. Each recording session was $\sim$40 min with 60.5 $\pm$ 5.49 stimulations per session but sessions varied depending on how long it took animals to completely explore the environment.

Histology

Immunocytochemistry was used to assess the virus distribution across the septum and localize tetrode recording sites in the MEC. Experimental animals were euthanized following experiments. Mice were anesthetized and intracardially perfused with 4% paraformaldehyde in PBS. Brains post-fixed by immersion in the same fixative for 2 weeks with the tetrodes in place following perfusion and then dissected from the skull. Free-floating coronal sections of the entire medial septum and sagittal sections of the entire entorhinal cortex were cut using a vibratome (40 μm) or on the cryostat (25 μm). Free-floating sections across the septum were incubated in GFP rabbit antiserum (1:1000, Invitrogen), and were detected with anti-rabbit coupled to Alexa Fluor 488 (1:1000, Invitrogen). Sections of the entorhinal cortex were stained for cresyl violet to located tetrode tips. The slices were mounted with Fluoromount-G (Southern

Biotechnology) and analyzed with an AxioObserver.Z1 microscope (Carl Zeiss). ImageJ was used to crop and decrease background for anatomical images included in the publication.

Data processing

Cluster cutting

Single-units were isolated 'offline' manually using graphical cluster cutting software (Offline Sorter, Plexon Inc.) individually for each recording session. Neurons were separated based on the peak amplitude and principal component measures of spike waveforms. Stability of units was confirmed by tracking waveform profiles across the four leads of the tetrode and cluster position across recording sessions, comparing to the baseline session.

Position estimation

To estimate the position of the animal, we measured the centroid of a group of red and green diodes positioned on the recording head stage. Head direction was calculated as the angle between the red and green diodes.

QUANTIFICATION AND STATISTICAL ANALYSIS

Data analysis

To analyze LFP power, the power spectrum for local field potentials was obtained using multitaper method included in the Chronux toolbox (mtspectrumc with NW = 3 and K = 5[51]. Theta power was calculated by taking the area within 1Hz of the maximum power in the theta range (6-10Hz). Baseline theta power was obtained by taking the average of theta power during laser-off trials, and mean reduction in theta power for each session was obtained by dividing each laser-on trial with baseline theta power and averaging across laser-on trials. For each channel, the theta-delta ratio was obtained by taking the ratio between mean theta power (6-10Hz) and mean delta power (2-4Hz) during laser-off segments. The channel with the highest theta-delta ratio was used in the LFP analysis.

Measurement of single unit properties

Spatial rate maps were constructed for a given unit by taking the number of spikes in 3.6 cm by 3.6 cm spatial bins and dividing by the amount of time spent in that bin. Rate maps were smoothed using a 5x5 bin 2D-Gaussian kernel with a one-bin standard deviation. The spatial periodicity of grid cells was quantified with a ''gridness'' score and computed from the spatial autocorrelation of the smoothed rate maps as described in Brandon et al., 2011.[9] In brief, to calculate the gridness score, ''gridness 3″ from Brandon et al.,[9] this score quantifies the hexagonal spatial periodicity of a firing rate map. It takes into account elliptical eccentricity along with one of two mirror lines that exist in a hexagonal lattice structure. Distortion along one of the mirror lines was corrected after determining the major and minor axes of the grid based on the six fields closest to the central peak of the rate map autocorrelogram. The entire autocorrelogram was compressed along the major axis so that the major axis is equal to the minor axis. Large eccentricities (where the minor axis was less than half of the major axis) were not corrected. From the compressed autocorrelogram, the center peak was removed, and the six surrounding peaks were identified found and cut out to make a donut. The rotational autocorrelation of this ring was then calculated as the periodicity in paired pixel correlations across 180 degrees of rotation. The correlation was calculated for each 3-degree rotation of the donut to itself. The gridness score is the difference between the correlation at the minimum peak of 60 or 120° and the maximum trough at 30, 90, or 150°. A negative gridness score indicates no measurable hexagonal spatial periodicity of the rate map. In line with Dannenberg et al.[52], grid cells were defined as cells with a grid score $\geq$0.19 and at least 300 spikes in the baseline condition. The spatial information of a cell was calculated using the same rate map as above, with the equation for I in bits/spike where p_i is the probability of occupancy in pixel i, F_i is the firing rate for pixel I, and F is the mean firing rate. Gridness evolution was calculated using a 30-s rolling window with 1-s steps beginning at 1 s following later onset. Baseline grid score values were calculated using 50 shuffled start times and both the recovery and baseline values were averaged over 2 s periods.

Grid cell phase precession was calculated using a 'pass index' analysis as described in Climer et al.[53] This method quantifies precession by evaluating the correlation between a cells' firing and the theta phase as the animal traverses a spatial field. Spatial field locations were identified using a 'field index' method, which calculates occupancy-normalized firing rates within each positional data bin. Field contours and centers were derived using various parameters related to the field index and firing rate. By analyzing the field index signal throughout a recording session, the mouse's entry and exit from a spatial field were estimated. The pass index was determined by normalizing segments of the field index signal, representing the mouse's passage through a spatial field, to a range of −1 to +1. Here, −1 indicates the start of a pass, 0 the center, and +1 the end. Spike phases during field crossings were aligned to this normalized position, and a linear-circular correlation was calculated between the field index and spiking phase. A grid cell showing a significant correlation ($p < 0.05$) and a per-pass slope between −1440 and −22 was classified as a phase-precessing cell.

Statistics

All statistical tests are noted where the corresponding results are reported throughout the results and figure legends. All tests were 2-tailed unless otherwise noted. Nonparametric tests were used as neural data violates the assumptions of parametric tests. All statistical evaluations were performed under MATLAB and Prism. No statistical methods were used to pre-determine sample sizes. Unless otherwise stated, nonparametric tests with a p value threshold of 0.05 were used for all statistical comparisons. Non-parametric Wilcoxon signed rank tests, Wilcoxon rank sum tests, Kolmogorov-Smirnov tests, and Kruskal-Wallis or Friedman tests one-way

ANOVAs were used throughout the paper. Mean and SEM or Median and IQR are provided for all distributions in which comparisons were made. *p*-values reported from all post hoc tests were with Dunn's multiple comparison test unless otherwise indicated. When *p* values are indicated in figures with $*p < 0.05$, $**p < 0.01$, $***p < 0.001$, $****p < 0.0001$ or the absolute *p* value is reported. Figures were constructed using Adobe Illustrator.